



Research



Cite this article: Walker AM, Davies CJ, Wilson AJ, Bergman MI. 2025 A non-equilibrium slurry model for planetary cores with application to Earth's F-layer. *Proc. R. Soc. A* **481**: 20240505. <https://doi.org/10.1098/rspa.2024.0505>

Received: 8 July 2024

Accepted: 3 March 2025

Subject Areas:

geophysics, fluid mechanics, thermodynamics

Keywords:

slurry, non-equilibrium, planetary cores, nucleation, crystal growth

Author for correspondence:

A. M. Walker

e-mail: andrew.walker@earth.ox.ac.uk

A non-equilibrium slurry model for planetary cores with application to Earth's F-layer

A. M. Walker¹, C. J. Davies², A. J. Wilson³ and M. I. Bergman³

¹Department of Earth Sciences, University of Oxford, South Parks Road, Oxford OX1 3AN, UK

²School of Earth and Environment, University of Leeds, Leeds LS2 9JT, UK

³Bard College at Simon's Rock, Great Barrington 01230, MA, USA

AMW, 0000-0003-3121-3255; CJD, 0000-0002-1074-3815; AJW, 0000-0002-6602-0990

Slurry regions may exist in the cores of several terrestrial bodies and are expected to influence the dynamics of deep planetary interiors and the viability of maintaining global magnetic fields. Here, we develop a two-component slurry model of the lowermost outer core of the Earth (the F-layer). In contrast to most previous models of slurries in planetary cores, we explicitly model the physics controlling the nucleation, growth and sinking of individual iron crystals and do not assume that the layer is in phase equilibrium. We assume that falling crystals do not interact and that the temperature and the overall composition are imposed, which allows us to solve for the volume fraction of solid in the layer and the size distribution of crystals. Models that produce a plausible heat budget and density excess compared with the bulk core yield a solid fraction that is far below that predicted by phase equilibrium and have a crystal size distribution dominated by the smallest particles with a maximum particle radii of 3 cm. The model can be used to understand the role of non-equilibrium effects in other planetary cores.

Electronic supplementary material is available online at <https://doi.org/10.6084/m9.figshare.c.7719725>.

1. Introduction

Interactions between solids and liquids are crucial for determining the thermal, chemical and magnetic evolution of the cores of terrestrial planets. Slow cooling of the Earth's liquid core combined with high pressure conditions leads to freezing at the planet's centre, with rejection of light elements from the solid providing a main power source for the modern geomagnetic field [1]. However, the nature of this freezing is debated, with suggestions including direct freezing and dendritic growth [2], heterogeneous freezing and melting leading to inner core translation [3–5], and the possibility that iron crystallizes and falls out of the liquid leading to growth by sedimentation [6,7]. By contrast, theoretical and experimental work suggest that the cores of smaller bodies, such as the Moon, Mars and Ganymede will freeze from the top down, producing a slurry layer near the top of the core in which a low volume fraction of heavy iron particles freeze out of the liquid and sink, remelting in the deeper core [8–14]. Modelling based on Fe–FeS alloys indicates that this 'iron snow' regime significantly affects core evolution, for example, through the formation of stable chemical stratification of S-rich liquid across the slurry layer and enhanced power for magnetic field generation arising from the sinking and remelting of solid particles [10,12].

Several studies have argued that another slurry region exists at the base of the Earth's liquid core [7,15–20], explaining a low-velocity layer above the inner core boundary (ICB). This low-velocity layer is a robust feature of seismic models of the outer core found in some one-dimensional reference models [21,22] with additional evidence coming from targeted studies of body waves that propagate through the deep outer core or diffract along the ICB (e.g. [23–27]). These studies, reviewed in [28], provide strong evidence that the lowermost 150 km [21,23] to 400 km [27] of the liquid core has anomalously low P-wave velocity. This differs from models such as PREM [29], which closely follow an adiabatic density profile to the ICB. The non-adiabatic P-wave velocity has been interpreted as a density stratification [6] of the liquid core. Here, we follow modern usage and call this layer the 'F-layer', noting that originally this term was used for a thinner and lower-velocity layer. The excess density in the F-layer challenges our understanding of the Earth's core because the light elements that are supposed to power field generation must be able to rise through the F-layer without disturbing the stratification.

The F-layer cannot be explained by a thermal boundary layer or a pure iron slurry [6], while a high solid fraction in the layer (reflecting a mushy zone) is also unacceptable as it would be seismically detected. Asymmetric melting and freezing of the inner core due to convective translation [3] may produce a dense layer of light-element-depleted fluid that envelops the inner core [4], which may explain the F-layer, though this requires a much lower inner core thermal conductivity than obtained by most recent studies (e.g. [30]) or some forcing from the outer core [31]. A slurry model of the F-layer is appealing because it predicts seismic velocities and density contrasts that are consistent with observations [19], while providing a self-consistent explanation for the flux of light elements into the overlying bulk core [7] and being compatible with the upward revision of the thermal conductivity of iron alloys [30,32,33]. In the model of Wong *et al.* [19], the temperature profile in the F-layer is destabilizing and hence the stratification is driven by a radial increase in oxygen concentration. However, in common with all current snow/slurry models of planetary cores, this slurry F-layer model assumes thermodynamic equilibrium: there is no barrier to the nucleation, growth or melting of solids in the liquid. Here we construct a non-equilibrium model of the F-layer, under the assumption that it represents a slurry, to explore how departures from equilibrium could influence our understanding of the dynamics and evolution of slurries in planetary cores.

The common assumption of phase equilibrium means that the solid volume fraction, ϕ , responds instantly to changes in temperature, T , pressure, P and composition of the liquid, X^L (where X^L is mole fraction with $X^L = 1$ indicating pure Fe and $X^L = 0$ pure FeO). This makes it possible to keep track of ϕ and thus the contribution of the slurry layer to the thermal evolution of the planet, but extraction of information such as the size and settling velocity of the crystals requires additional assumptions [10]. Solomatov & Stevenson [34] developed a theory for crystal

nucleation and growth in a vigorously convecting silicate magma ocean, but this does not readily translate to the fundamentally different conditions in planetary cores. Loper [35] produced a non-equilibrium slurry theory by introducing a parameter to allow for small deviations from equilibrium, which represents the physics occurring at the scale of single iron particles below the continuum scale adopted by the rest of the theory. However, this approach has not been used to explore the behaviour of planetary cores.

In this paper, we develop a non-equilibrium model of the Earth's F-layer as an iron snow zone built from the behaviour of single iron particles as they grow and fall towards the ICB (figure 1). We consider the combined effect of nucleation and growth as well as the important coupling between the fluid dynamics of falling particles and the thermodynamics of a two-phase region. Our model does not impose thermodynamic equilibrium (although solutions may be in equilibrium) and yields rich information on the state of the layer. In §2, we describe a thermodynamic model of the Fe–FeO system, valid at the high P and T conditions of the Earth's core, which is used to determine the chemical potential differences that drive particle nucleation and growth and the extent of departures from equilibrium. This choice of chemistry (which can be easily changed in our implementation) is consistent with the seismically inferred density difference between the inner and outer core [36] and allows us to neglect the possibility of light elements partitioning into the solid phase, which also proves to be a useful simplification. In §3, we detail the processes considered to determine the fluid dynamics of a single pre-existing iron particle, the particle's falling velocity and properties of the momentum and compositional boundary layers that develop in the liquid adjacent to the solid interface, and how these couple to the particle growth. This treatment of iron particles involves additional assumptions: principally that the fluid in the slurry layer is density stratified, that particles are spherical and that they do not interact with each other either via physical collisions or induced fluid flow. In §4, we describe how we consider the formation of solid particles within the slurry and involves the assumptions of classical nucleation theory (CNT) (where we find it necessary to invoke pre-existing 'dust' as nucleation sites). In §5, we describe the collective behaviour of particles as they nucleate and grow while falling through the F-layer within a one-dimensional model. This involves the imposition of a temperature and compositional profiles for the liquid and the implicit assumption that the processes governing the approach to equilibrium in the F-layer occur on a timescale much faster than secular changes to the temperature or composition of the overlying outer core. This one-dimensional model produces a size distribution, number density and lifespan of groups of solid particles that nucleate at a particular radius and fall through the F-layer. From this information, we compute the growth rate of the inner core (with the assumption that the inner core only grows by sedimentation of falling particles) alongside the density profile (including contributions from the solid volume as well as the composition and temperature of the liquid) and heat production in the layer that is released upwards into the outer core. Finally, in §6, we search for models that match constraints from seismology and the thermal evolution of the Earth, describe the kinds of solutions that are acceptable within these constraints, and consider potential extensions of this work to other planetary cores and paths to the lifting of some key assumptions and integration of our results within other models of the core.

2. An iron–oxygen thermodynamic model for the F-layer

In common with most existing models of slurries in planetary cores, we start by simplifying the composition of the core and consider an alloy of iron and a light element which partitions strongly into the liquid phase on crystallization. In the limit of complete partitioning this approximation (the 'constant solid composition' approximation of Loper & Roberts [17]) means there is no need to track the composition of the solid in the slurry. For Earth, oxygen is a common choice of light element [32] because it is cosmochemically abundant, expected to partition into the core during planetary differentiation and, as opposed to S and Si, is likely to produce a density jump at the ICB as required by seismology [37]. Komabayashi [38] produced a thermodynamic description of an Fe–FeO alloy system at high temperature and pressure that is suitable for use in our model

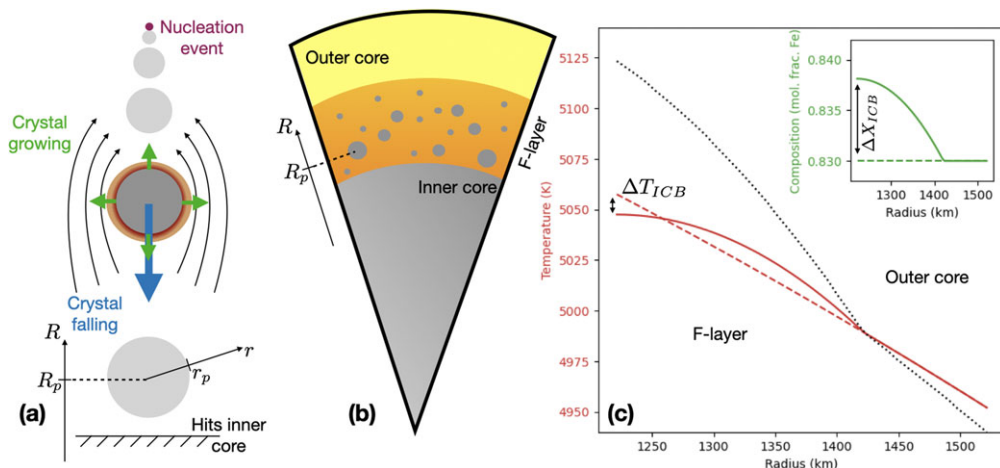


Figure 1. Illustration of the model set-up. We focus on the small-scale physics controlling the formation, falling and growth of single iron crystals (a) before combining these into a model of the collective behaviour of the F-layer (b). We illustrate the two one-dimensional coordinate systems used in this work. One (denoted r) has an origin at the centre of a single particle with radius r_p . The second (R) has an origin at the centre of the Earth with a particle position denoted R_p (a full list of the symbols used throughout this paper can be found in the electronic supplementary material). Example temperature (red lines) and compositional (green lines) profiles relevant to this layer are shown in (c) alongside the liquidus temperature (black dotted line). In the outer core above the F-layer, the composition is constant and the temperature follows an adiabatic profile (these are extrapolated as dashed lines inside the F-layer). The temperature intersects the liquidus at the top of the 200 km thick F-layer and below this the composition and temperature are parametrized by a second-order polynomial that differs by ΔT_{ICB} and ΔX_{ICB} from the extrapolation at the ICB.

and in which oxygen does not enter the solid iron phase. However, we note that it is not possible for the core to be formed entirely of an Fe–O alloy as this does not account for the density of the inner core and the eutectic for this system is colder than the expected temperature of the ICB. Nevertheless, the simple system is well suited to our needs and demonstrates the power of the model we develop.

At equilibrium, slurry layers in metallic planetary cores can exist over a range of pressure–temperature conditions because of the presence of two-phase regions in metal alloy phase diagrams. An example for the prototypical Fe–FeO system calculated for plausible F-layer pressure–temperature–composition conditions is shown in figure 2. The equilibrium assemblage for a composition that falls within the region bounded by the liquidus, the solidus and the eutectic temperature (marked ‘two-phase region’) will, on the terrestrially relevant Fe-rich side of the eutectic point considered here, be a mixture of solid iron and a liquid Fe–O alloy with composition enriched in O compared with the bulk. We use the thermodynamic model of Komabayashi [38] to describe the free energy of pure solid Fe, stoichiometric FeO and an Fe–O liquid. In this model, the volumes of the end-members are described by the Vinet–Anderson–Grüneisen equations of state to capture the effect of pressure and pressure-dependent thermal expansion. This yields the end-member molar volumes and thus the densities of the (pure iron) solid, ρ^S , and of liquid Fe and FeO all as a function of P and T . These are combined with a polynomial representation of the free energies as a function of temperature at fixed volume to give the chemical potential of iron in the end-members, $\mu_{Fe}^S(P, T, X^S = 1)$ and $\mu_{Fe}^L(P, T, X^L = 1)$. Liquid Fe and FeO (under these high-pressure conditions) are assumed to form an ideal solution [38] and therefore the liquid density, ρ^L , for any composition X^L , is found by linearly interpolating between end members and the chemical potential difference between solid and liquid is

$$\Delta\mu_{Fe}(P, T, X^L) = \mu_{Fe}^S(P, T, X^S = 1) - [\mu_{Fe}^L(P, T, X^L = 1) + R_g T \ln X^L], \quad (2.1)$$

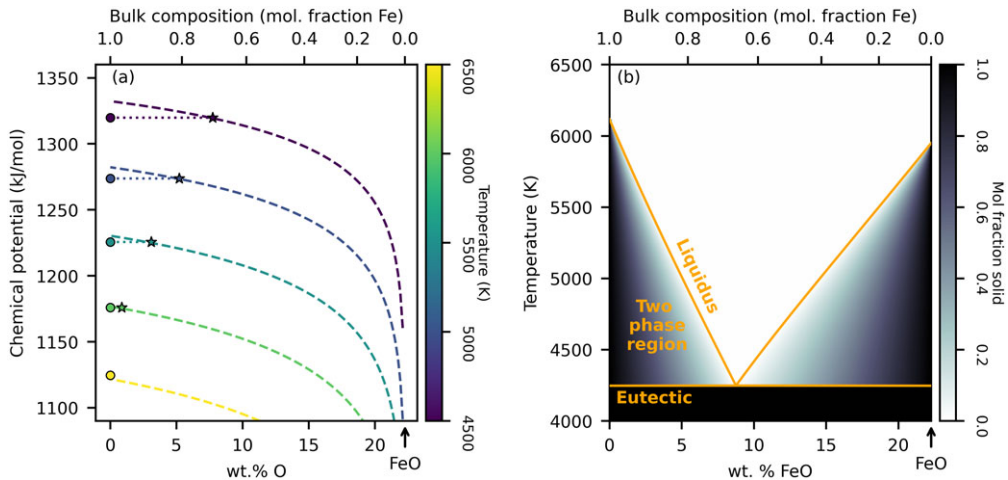


Figure 2. Equilibrium properties of the Fe–FeO system computed from [38] at 330 GPa. (a) The chemical potential of liquid FeO mixtures (dashed lines) and the pure solid Fe chemical potential (circles) coloured by temperature. Dotted tie lines connect solid Fe with the equilibrium liquid mixture for temperatures within the two-phase region. At 6500 K solid Fe is unstable compared to a pure Fe liquid. (b) Calculated phase diagram where phase boundaries (liquidus and eutectic) are shown (orange lines) and the solid Fe–liquid FeO two-phase region relevant to our slurry model is labelled. The equilibrium solid fraction is indicated by the shading.

where R_g is the gas constant and the final term represents the entropy of mixing (with the positive sign resulting from a decrease in entropy with increasing iron content in the liquid). To efficiently evaluate the volume of each phase (and thus the densities and chemical potential) as a function of pressure, we use an approximate inverse of the Vinet equation of state to avoid the need for a numerical solution at each pressure [39]. As shown in figure 2, for a given range of pressures and temperatures, the iron fraction of the liquid, X^{eq} , in equilibrium with solid iron can be found from this thermodynamic model by searching for the composition where $\Delta\mu_{\text{Fe}}(P, T, X^{\text{L}}) = 0$. This defines the liquidus.

For a given composition of the liquid and bulk composition, X^{tot} , it is possible to evaluate the mole fraction solid, \mathcal{X} , by conserving the total composition of the system:

$$\mathcal{X} = 1 - \frac{1 - X^{\text{tot}}}{1 - X^{\text{L}}}. \quad (2.2)$$

Setting $X^{\text{L}} = X^{\text{eq}}$ in equation (2.2) yields the lever rule and the equilibrium mole fraction solid, \mathcal{X}^{eq} . This is shown by the shading in figure 2 and the difference between \mathcal{X} and \mathcal{X}^{eq} is one way to measure departure from equilibrium. Since we know the volumes of the components, it is straightforward to convert from \mathcal{X} (and \mathcal{X}^{eq}), to volume fraction solid, ϕ , and the equilibrium volume fraction solid, ϕ^{eq} , which are more amenable to calculation. An analogous approach can be used to probe the FeO side of the phase diagram. While this is unlikely to be directly relevant to the F-layer, it may pertain to small planetary bodies, such as Ganymede [40].

The equilibrium thermodynamics summarized above allow the relationship between solid fraction, composition, temperature and pressure to be described in models of slurries. This amounts to models where the temperature and pressure define the composition of the liquid or, equivalently, where knowing the composition and pressure defines the temperature via a liquidus relation. Because this equilibrium is maintained by the rapid creation or removal of solid, this approximation is often known as the ‘fast melting’ approximation [17], and it is this that allows a parametrized liquidus (rather than a thermodynamic description of melting) to appear in slurry models [7,10,12,19]. It is this approximation that we seek to lift. We can do this because, as well as allowing the calculation of the equilibrium phase diagram, a thermodynamic model

provides access to the driving force, $\Delta\mu_{\text{Fe}}$, for the processes which determine how quickly a non-equilibrium system will move towards equilibrium. In a slurry with smaller ϕ than predicted by equation (2.2), large negative values of $\Delta\mu_{\text{Fe}}(P, T, X^{\text{L}})$ will tend to drive faster growth and higher nucleation than small values, but this driving force must compete with kinetic effects (diffusion and collision rate of atoms), and can only operate for a limited time period while any solid falls out of the liquid. This makes the thermodynamic model summarized in equation (2.1) key to our non-equilibrium description of the F-layer, despite the fact that the model is parametrized, in part, to reproduce equilibrium experiments.

3. A model of a falling growing iron particle

Before describing the properties of the whole slurry layer, we develop a model of a single solid iron particle falling through a stationary liquid-iron alloy within the two-phase region. The rate dr_p/dt at which a spherical particle of radius r_p grows or shrinks as it falls controls how quickly it can contribute to phase equilibrium within the layer while its falling velocity w_p ($= -(dR_p/dt)$ as R increases upwards) controls how long it has to contribute to this process. Because of the physical processes described below we expect the falling velocity to depend on the particle size and the growth rate to depend on the falling velocity, so we evolve the position and size of the particle together by integrating a pair of coupled ordinary differential equations (ODEs). Our task is to describe the coupling of R_p and r_p and to evaluate $R_p(t)$ and $r_p(t)$, where time, t , is measured from the instant the particle first forms. Throughout, we assume that the F-layer is stratified, that the total solid fraction is low (so particles do not interact via collisions or by closely approaching each other; this is expected in a slurry) and that thermal diffusion is sufficiently fast [41] to maintain thermal equilibrium (such that we can impose the temperature). For the purpose of this section (where we only consider a single iron particle), we impose constant temperature, pressure and liquid composition, although we allow these to vary with R in later sections.

(a) Falling velocity

Time-dependent three-dimensional solutions of the Navier–Stokes equations for a fluid containing a large number of solid particles are computationally inaccessible at the conditions of planetary cores. To enable a flexible and fast representation of solid–liquid fluid dynamical interactions, we therefore use scaling laws that describe the gross properties of the particle velocity and the boundary layers surrounding falling particles.

Particles in the slurry are assumed to be more dense than the stratified liquid and will quickly accelerate to fall at their terminal velocity. The simplest estimate of the particle velocity is based on Stokes' flow, which gives the terminal velocity of the particle by balancing buoyancy and drag forces and applies at low Reynolds number, Re , defined as

$$Re = \frac{2r_p|w_p|}{\nu^{\text{L}}}, \quad (3.1)$$

where ρ^{L} and ν^{L} are the liquid density and kinematic viscosity, respectively. In this classical regime $w_p = w_{\text{stokes}} = (2/9)(\rho^{\text{S}} - \rho^{\text{L}})gr_p^2/(\nu^{\text{L}}\rho^{\text{L}})$, where g is gravity. As w_p (and Re) increases, the drag experienced by the sphere is enhanced compared to the Stokes solution. We use an empirical relation for the drag coefficient valid for $Re \leq 3 \times 10^5$ [42–44],

$$C_D = \frac{24}{Re} \left(1 + 0.15Re^{0.687} \right) + \frac{0.42}{1 + 42500Re^{-1.16}}, \quad (3.2)$$

in terms of which the falling velocity is

$$w_p = -\frac{dR_p}{dt} = \sqrt{\left(\frac{8(\rho^{\text{S}} - \rho^{\text{L}})gr_p}{3\rho^{\text{L}}C_D} \right)}. \quad (3.3)$$

Because Re depends on w_p , equations (3.1) and (3.3) are solved self-consistently as described in [44].

To represent the boundary-layer dynamics, we first note that the compositional boundary layer in the solid and the thermal boundary layers on either side of the particle–fluid interface are absent by assumption. The momentum boundary thickness in the liquid, δ_u , is required to determine the thickness of the chemical boundary layer in the liquid, δ_C . To describe δ_u and δ_C , we use results from Inman *et al.* [45], who numerically simulated the incompressible axisymmetric flow arising from an isolated particle sinking through a stabilizing linear chemical gradient. A stabilizing background gradient has been obtained in recent equilibrium models of the F-layer [19] and snow zones [10]. In this configuration, the dynamics are described by the Schmidt, chemical Péclet and Froude numbers, which are defined, respectively, as

$$Sc = \frac{\nu^L}{D^L}, \quad Pe_C = \frac{2r_p |w_p|}{D^L} = Sc Re \quad \text{and} \quad Fr = \frac{|w_p|}{N_{BV} r_p}, \quad (3.4)$$

where D^L is the oxygen diffusion coefficient in the liquid and N_{BV} is the Brunt–Väisälä frequency

$$N_{BV}^2 = -\frac{g}{\rho} \frac{\partial \rho'}{\partial r} \approx -\frac{g_m}{\rho_m} \frac{\rho'_t - \rho'_b}{R_t - R_b}, \quad (3.5)$$

which increases as the layer becomes more strongly stratified. Here ρ' is the density deviation from the adiabatic and chemically well-mixed state and the right-hand side approximates N_{BV} by quantities in the middle (subscript m), top (subscript t) and base (subscript b) of the layer. In the geophysically relevant limit of $Sc \gg 1$ [41], the regimes depend on Fr and Re . At high Fr (weak stratification) and $Re < 10^{-2}$, the momentum boundary layer is weak or absent because advection cannot balance viscous diffusion in the boundary-layer equation, and the only length-scale in the problem is $2r_p$. The results of Inman *et al.* [45] suggest that the chemical boundary is also weak or absent at $Pe_C \sim 10$, which corresponds to $Re \sim 10^{-2}$ for $Sc \sim 1000$. At higher Pe_C a chemical boundary layer of thickness δ_C at the particle equator develops in which the chemical advection and diffusion are approximately in balance. The mechanical boundary thickness δ_u depends on Re : $\delta_u/2r_p \sim 1$ at $10^{-2} \leq Re \leq 10^2$ (see fig. 7b of [45]); $\delta/2r_p \sim Re^{-0.5}$ for $Re > 200$, i.e. the classical balance between viscosity and inertia. In the low Fr (strong stratification) regime, the same logic is applied except that for $Re \geq 10^{-2}$, δ_u is estimated based on a balance between viscosity and buoyancy in the momentum equation [45]. With these considerations, the chemical boundary-layer thicknesses in the weak stratification ($Fr > 10$), regime are

$$\begin{aligned} 2r_p & & Re < 10^{-2}, \\ \delta_C = 0.215 Re^{-1/3} 2r_p & & 10^{-2} \leq Re \leq 10^2, \\ 0.464 Re^{-1/2} 2r_p & & Re > 10^2, \end{aligned} \quad (3.6)$$

while in the strong stratification regime ($Fr \leq 10$) they are

$$\begin{aligned} 2r_p & & Re < 10^{-2}, \\ \delta_C = 0.1 Re^{-1/2} 2r_p & & Re \geq 10^{-2}. \end{aligned} \quad (3.7)$$

In these equations, the pre-factors are determined by continuity of mechanical and compositional boundary-layer thicknesses at the regime boundaries as in [46].

Calculated falling velocities, boundary-layer thickness and scaling regime information are shown as a function of r_p for solid and liquid properties expected close to the ICB in figure 3. From the nanometre size expected after nucleation, small particles experience laminar flow, have a relatively large boundary-layer thickness and fall at the classical Stokes velocity. As the particle grows to the 10–100 μm range it enters the intermediate Re regime, develops a relatively thinner boundary layer and gradually slows down compared with the Stokes prediction. The deviation between the Stokes falling velocity and the self-consistent calculation is clear by the time the particle grows to millimetre size and enters the high Re regime. For these parameters, if the particle were to grow beyond 25 cm the empirical drag coefficient would no longer be valid. This corresponds to falling velocities in the m s^{-1} range, where particles traverse the whole F-layer in

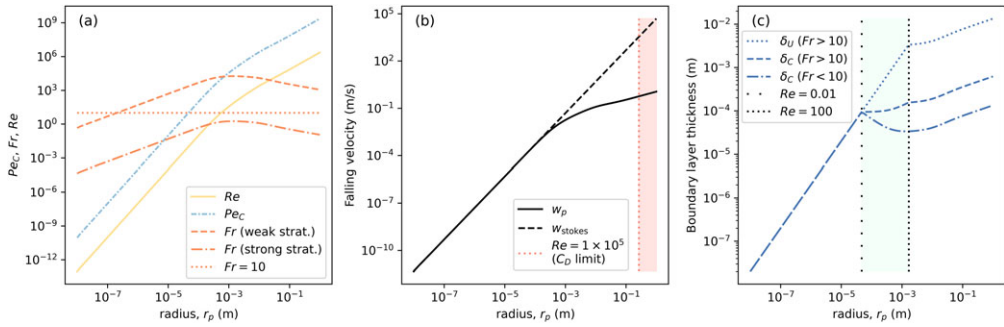


Figure 3. Dynamical regime, falling velocity and boundary-layer thickness for an iron particle falling through a stratified liquid with parameters relevant to the F-layer ($\rho^S = 12\,700\text{ kg m}^{-3}$, $\rho^L = 12\,100\text{ kg m}^{-3}$, $g = 4.4\text{ m s}^{-2}$, $D^L = 1 \times 10^{-9}\text{ m}^2\text{ s}^{-1}$ and $\nu^L = 1 \times 10^{-6}\text{ m}^2\text{ s}^{-1}$). (a) Re (yellow) and Pec (blue) and Fr (orange, dashed for $N_{BW} = 10^{-3}\text{ Hz}$ and dash-dots for $N_{BW} = 10\text{ Hz}$) are calculated self-consistently and determine the dynamical regime, with $Fr = 10$ indicated. (b) Falling velocity (solid line) and Stokes velocity (dashed line) showing the divergence at larger particle radii. The vertical line and pink shading corresponds to $Re \geq 3 \times 10^5$, the upper bound on the empirical scaling for the drag coefficient. (c) Momentum (dotted line) and chemical (dashed for $N_{BW} = 10^{-3}$ and dash-dots for $N_{BW} = 10\text{ Hz}$) boundary-layer thickness. Vertical dotted lines showing the intermediate and large Re regime transitions.

a few days. Figure 3 also shows the difference in boundary-layer behaviour for a particle falling through a weak chemical stratification (high Fr , $N_{BW} = 10^{-3}\text{ Hz}$) and a strong stratification (low Fr , $N_{BW} = 10\text{ Hz}$). For the Earth, the difference between PREM (which has an adiabatic density in the outer core [29]) and AK135f (where the base of the outer core shows stable stratification, [47]) predicts $N_{BW} \sim 1 \times 10^{-4}\text{ Hz}$ at the base of the F-layer. We thus expect boundary layers for particles to be more accurately represented by the weakly stratified (low Fr) scaling.

(b) Growth rate

The rate of particle growth depends primarily on three factors: the thermodynamic driving force $\Delta\mu_{Fe}$; surface kinetics, reflecting the fact that particles cannot grow faster than the rate at which atoms arrive at the interface and arrange themselves into the solid structure; and, compositional variations in the adjacent liquid. The first two factors are typically described by models of the form

$$\frac{dr_p}{dt} = k(T) \left[1 - \exp\left(-\frac{\Delta\mu_{Fe}(P, T, X^L)}{R_g T}\right) \right], \quad (3.8)$$

where $k(T)$ is a kinetic function, and $\Delta\mu_{Fe}$ is defined in equation (2.1). Zero growth rate occurs at equilibrium, i.e. when $\Delta\mu_{Fe} = 0$.

The growth rate of iron under core conditions, and thus the appropriate parameters of equation (3.8) are not known. There are at least three groups of theories for $k(T)$ for pure metals, those which assume diffusion controlled kinetics [48,49], those which assume collision-controlled kinetics [50] and those which assume density fluctuations in the liquid control the kinetics of growth [51]. Atomic scale simulations of six *fcc* metals suggests that a temperature-independent kinetic factor (i.e. $k(T) = k_0$) with large magnitude ($140\text{--}650\text{ m s}^{-1}$) gives a good description of the growth kinetics to large undercooling [52], and we assume similar behaviour holds for *hcp* iron at ICB conditions. However, in our two component system it is evident that movement of oxygen away from the growing interface must play a role. Oxygen will need to diffuse through the boundary-layer set-up by the falling particle and the thickness of this layer depends on the particle size as discussed above. Existing theories appealing to diffusion to define $k(T)$ are not well suited to this situation, so we proceed by separating the kinetic control on particle growth into two contributions setting $k(T) = k_0$ [52] and treating oxygen diffusion separately.

Compositional variations in the boundary layer arise due to the exclusion of oxygen from the solid as the particle grows. As described in the electronic supplementary material, conservation of mass leads to a relationship between the particle growth rate and the gradient of the composition of the liquid at the particle interface:

$$\left. \frac{dX(r)}{dr} \right|_{r=r_p} = \frac{X(r_p)}{D^L} \frac{dr_p}{dt}. \quad (3.9)$$

Supported by the results of Inman *et al.* [45], we assume that the boundary-layer structure is linear, increasing from $X(r_p)$ at the interface to the bulk liquid composition, $X(r_p + \delta_C) = X^L$, at and beyond the outer edge of the boundary layer. Using equation (3.8), equation (3.9) becomes

$$\left. \frac{dX(r)}{dr} \right|_{r=r_p} \approx \frac{X^L - X(r_p)}{\delta_C} = \frac{k_0 X(r_p)}{D^L} \left[1 - \exp\left(\frac{\Delta\mu_{\text{Fe}}(P, T, X(r_p))}{RT}\right) \right]. \quad (3.10)$$

For a given δ_C (which does not depend on $X(r)$) and X^L , this relation determines the particle growth rate that is consistent with the liquid composition and its gradient at the interface.

Figure 4a shows the variation in growth rate as a function of solid fraction with fixed bulk composition for different values of k_0 using equation (3.8). At $\phi = 0$, $\Delta\mu_{\text{Fe}}$ is large and negative and the growth rate is set by k_0 . Increasing the solid fraction evolves the system towards the equilibrium composition at which point all curves reach zero growth rate ($\Delta\mu_{\text{Fe}} = 0$), which occurs at a single composition at the fixed P and T conditions shown. The compositions highlighted in figure 4a are used in figure 4b,c to demonstrate the variation of dr_p/dt and $X(r_p)$ with boundary-layer thickness as determined by equation (3.10). To understand the behaviour, it is helpful to combine equations (3.8) and (3.10) into the form

$$X^L = X(r_p) \left[1 + \frac{\delta_C}{D} \frac{dr_p}{dt} \right] \quad (3.11)$$

and note that, in this analysis, dr_p/dt is a function only of $X(r_p)$ because P and T are fixed (see the definition of $\Delta\mu_{\text{Fe}}$ in equation (2.1)). At small δ_C , the first term in brackets in equation (3.11) is dominant, implying $X(r_p) \sim X^L$ and a fast growth rate. As δ_C is increased at fixed D the two terms in the brackets in equation (3.11) become comparable, requiring $X(r_p)$ to decrease compared with X^L , which reduces the growth rate as shown in figure 4b,c. Physically, the large growth rate that arises when the system is far from equilibrium is associated with large diffusive flux across the chemical boundary layer, which is required to bring the system towards equilibrium. At equilibrium $dr_p/dt = 0$ and $X^L = X(r_p)$ corresponding to zero diffusive flux.

(c) A single falling and growing particle

The time evolution of the size and position of a falling particle is described by the pair of coupled ODEs (equations (3.3) and (3.9)) for a particle that starts with initial radius r_0 at position R_0 . We solve these together as an initial value problem making use of the ‘RK45’ Runge–Kutta method [53] as implemented in the SciPy library [54], where the dynamical time stepping is essential to efficient solution. In detail, at each Runge–Kutta step the growth rate and falling velocity is found as follows:

- (i) Calculate ρ^S , ρ^L and $\Delta\mu_{\text{Fe}}$ from T , P and X^L as outlined in §2.
- (ii) Self-consistently solve equations (3.1)–(3.3) to find Re and the particle falling velocity, $-(dR_p/dt)$.
- (iii) Calculate the thickness of the chemical boundary layer from equation (3.6).
- (iv) Self-consistently solve equations (3.8)–(3.10) to find the growth rate, dr_p/dt , and liquid composition at the interface.
- (v) With dR_p/dt and dr_p/dt in hand, update the position and size of the falling particle.

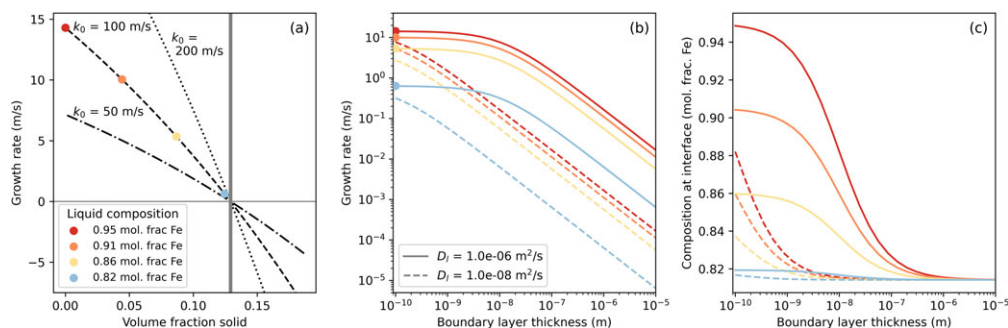


Figure 4. Calculated particle growth rate dr_p/dt for bulk composition $X^{\text{tot}} = 5 \text{ mol. \% O}$, $T = 5000 \text{ K}$ and $P = 330 \text{ GPa}$. Panel (a) shows dr_p/dt as a function of solid fraction ϕ , neglecting boundary-layer effects, using equation (3.8). Vertical grey line denotes the equilibrium solid fraction at the chosen $P - T - X^{\text{tot}}$. Coloured symbols denote the liquid composition calculated from equation (2.2) for the given ϕ and X^{tot} . Panels (b,c) show dr_p/dt and $X(r_p)$ as a function of fixed boundary-layer thickness using the four liquid compositions marked in (a) calculated with equation (3.10). Two values of the oxygen diffusivity are shown in solid and dashed lines. All coloured cases have k_0 set to 100 m s^{-1} .

This process ends when the particle hits the ICB and yields interpolating polynomials describing the particle position and size, $R_p(t; R_0, r_0)$ and $r_p(t; R_0, r_0)$, as a function of time, where we explicitly represent the dependence on initial conditions following the semi-colon. These functions can be used to easily find the particle size as a function of position, $r_p(R_p; R_0, r_0)$. In addition to the thermodynamic parametrization, this calculation requires knowledge of pressure, temperature, acceleration due to gravity, liquid viscosity, chemical diffusivity, the pre-factor for growth and the composition of the liquid outside the boundary layer. Our implementation allows these to be fixed or to vary with R . Solutions for some cases with fixed parameters approximately corresponding to the F-layer on Earth are shown in figure 5.

Particle evolution can be summarized by the transit time (the time taken to fall 200 km from the top to the bottom of the F-layer) and the final particle size just before it hits the ICB. The effect of two major controls on these summary measures, the liquid viscosity and oxygen diffusivity, are shown in figure 5b. As oxygen diffusivity increases the particles grow faster and thus fall faster, giving smaller transit times and larger final sizes. This can be seen by tracking any set of data points at fixed viscosity. Increasing the viscosity at fixed oxygen diffusivity results in solutions that follow curved lines of fixed colour across figure 5c. As expected, increasing the viscosity increases the drag, decreases the falling velocity and thus increases the transit time. However, for solutions with fixed oxygen diffusivity the final particle size is approximately independent of viscosity: the decreased falling velocity is balanced by a decreased growth rate. This can be explained by noting that, to leading order, D^L and δ_C scale in the same way with Re and thus viscosity.

Having considered the controls on the evolution of a single iron particle, we now focus on particle nucleation before considering how they behave en-mass within the F-layer.

4. Nucleation

No model of a core slurry zone is complete without consideration of how the solid particles form, and this process is particularly important in allowing deviation from equilibrium. The basic approach involves CNT, which accounts for the need for a liquid to cool sometimes significantly below its melting point (or liquidus temperature) before a solid can form [55]. The key idea is that spontaneous perturbations in the structure of the supercooled liquid will result in the formation of a nucleus of solid sufficiently large that the energy released on freezing (which scales with the volume of the nucleus) overcomes the energy penalty that accompanies the formation of

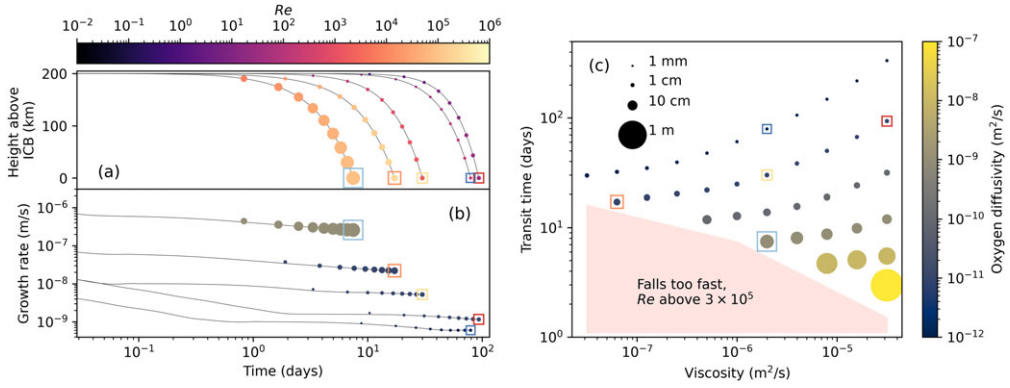


Figure 5. Summary of iron particle evolution during the process of falling through a 200 km thick layer of liquid iron containing 5 mol. % oxygen. Pressure is 330 GPa, temperature 5500 K, gravitational acceleration 5 ms⁻² and the initial particle size is 10⁻⁸ m. The position (a) and growth rate (b) of particles as a function of time as they fall through liquids with five different oxygen diffusivities and viscosities are shown with particle size indicated by symbol size (key in panel c) and Re indicated by colour in (a; top colour bar). The colour of the squares around the terminal symbols indicate oxygen diffusivities (red, orange and yellow: $D^L = 1 \times 10^{-11}$; light blue: $D^L = 1 \times 10^{-9}$; dark blue: $D^L = 1 \times 10^{-12}$ m² s⁻¹) and viscosities (yellow, dark blue and light blue: $\nu^L = 2 \times 10^{-6}$; red: $\nu^L = 3 \times 10^{-5}$; orange: $\nu^L = 6 \times 10^{-8}$ m² s⁻¹). Results from a larger set of input parameters are summarized in terms of the total transit time of the particle and its final size in (c) with the five cases shown in (a) and (b) highlighted by the same coloured squares. The symbol colours in (b) and (c) indicate oxygen diffusivity according to the colour bar on the right-hand side of the figure.

an interface between the new solid and liquid (which scales with surface area). For a spherical nucleus of radius r , the energy change is

$$\Delta G(r, P, T, X^L) = \left[\frac{4}{3} \pi r^3 g_{sl}(X^L, P, T) + 4 \pi r^2 \gamma \right] S(\theta), \quad (4.1)$$

where $g_{sl} = \Delta \mu_{Fe}(P, T, X^L)(\rho^L/56)$ is given by equation (2.1) (in units of energy per unit volume), γ is the excess energy caused by forming a solid–liquid interface (in units of energy per unit area) and the factor of 56 is the molar mass of iron. The function $S(\theta) = [2 - 3 \cos(\theta) + \cos^3(\theta)]/4$, where θ is the wetting angle between the solid and the liquid, permits the consideration of heterogeneous nucleation (where a pre-existing solid exists) considered below. For homogeneous nucleation (formation of new solid without a pre-existing solid surface), $\theta = 180^\circ$.

The critical size r_c beyond which a spontaneously formed spherical nucleus will be more likely to grow than dissolve corresponds to the maximum of ΔG :

$$r_c(P, T, X^L) = \frac{-2\gamma}{g_{sl}(P, T, X^L)} \quad (4.2)$$

and has energy

$$G(r_c(P, T, X^L)) = \frac{16\pi\gamma^3}{3g_{sl}(P, T, X^L)^2} S(\theta). \quad (4.3)$$

Heterogeneous nucleation reduces the energy barrier at r_c for small wetting angles, such as those typically found in metals [56].

Given a pre-factor that describes the rate at which liquid ‘attempts’ to form solid, I_0 , CNT allows the calculation of the nucleation rate, I :

$$I(P, T, X^L) = I_0 \exp \left[\frac{-\Delta G(r_c(P, T, X^L))}{k_b T} \right], \quad (4.4)$$

at which new crystals of the critical radius form, where k_b is Boltzmann’s constant. On average, half of these will rapidly dissolve, while the other half grow. The mean waiting time between

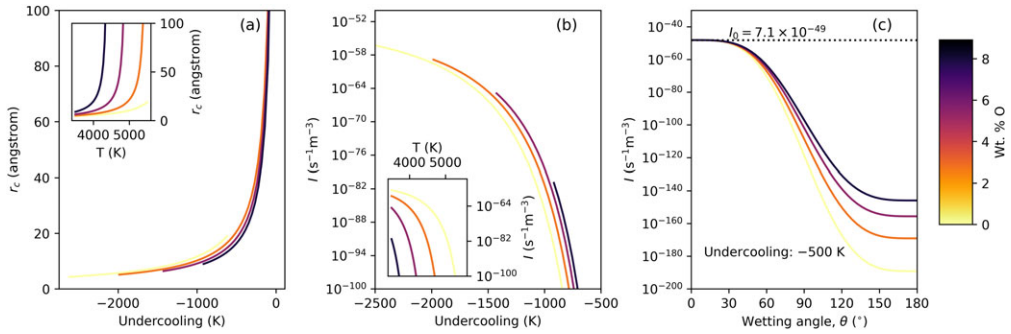


Figure 6. Critical nucleus size (a) and nucleation rate (b) for iron in an iron–oxygen supercooled liquid as a function of temperature and liquid composition. Calculations are performed at 330 GPa, with $\gamma = 1.08 \text{ J m}^{-2}$, and $I_0 = 7.1 \times 10^{-49} \text{ s}^{-1} \text{ m}^{-3}$ [57]. In the main plots, the temperature is shown in terms of undercooling below the liquidus temperature for each composition, while the insets show the same data in terms of absolute temperature which spreads out the curves (see text). The effect of wetting angle, θ for heterogeneous nucleation is shown in (c) for fixed 500 K undercooling. The nucleation rate approaches I_0 for small θ .

nucleation events in a volume element in the F-layer, with volume $V(R)$, is

$$\tau(R, P, T, X^L) = \frac{2}{I(P, T, X^L)V(R)}. \quad (4.5)$$

The expected nucleation rate and critical size for representative conditions are shown in figure 6.

CNT, as illustrated by figure 6, predicts a low probability of forming new solid particles in the F-layer by homogeneous nucleation, consistent with the findings of Shimizu *et al.* [58] who take this as support for a mush layer at the ICB. This is reminiscent of the ‘core nucleation paradox’, where CNT predicts that the combination of the time, volume and undercooling available on Earth is insufficient to permit the inner core to form [56,57,59–61]. Our estimate of the nucleation rate, using free energy changes derived from the thermodynamic model, accords with previous estimates based on the available metallurgical data [56] and atomic-scale simulation with [57], or without [59], substantial temperature extrapolation. There are two important differences between the situation for a two-component slurry and previous work considering the initial formation of the inner core. The first arises from the existence of a two-phase region in the phase diagram (figure 2). This allows substantial undercooling below the liquidus to drive nucleation without resulting in a situation where all the undercooled liquid freezes once the first solid forms. The second difference is due to the use of a full thermodynamic model and the interplay between this and the depression of the liquidus by the addition of oxygen. In absolute terms (i.e. fixing the temperature and increasing the oxygen content of the liquid), adding oxygen dramatically decreases the nucleation rate because it lowers the free energy of the liquid (seen in the inset to figure 6b). If instead we think in terms of undercooling below the liquidus, we find that nucleation rate is almost independent of oxygen content but that at fixed undercooling adding oxygen slightly increases the nucleation rate (shown in the main panel of figure 6b). This is because the temperature dependence of $\Delta\mu_{\text{Fe}}(P, T, X^L)$ is itself dependent on temperature and liquid composition [38]. This effect discounts any change in the composition of the liquid caused by the nucleation event, and neither effects are significant enough to change the argument that nucleation from a homogeneous liquid is unlikely.

One resolution, which at least allows us to explore the behaviour of a slurry in the F-layer, is to appeal to heterogeneous nucleation where iron particles nucleate on some pre-existing solid. From geometrical arguments [55], a simple model of this process can be parametrized by $S(\theta)$ in equation (4.1). The wetting angle for pre-existing oxides is expected to be more than 110° , while for metals it may be less than 25° [56]. Figure 6c shows the effect of wetting angle on

nucleation rate, with the homogeneous case reproduced for $\theta = 180^\circ$ and an enormous (100 order of magnitude) increase in nucleation rate with decreasing θ (i.e. for cases where the pre-existing solid is structurally and chemically similar to solid iron). At $\theta = 0^\circ$, the nucleation rate is entirely controlled by I_0 , which is itself highly uncertain. For nucleation of the inner core, finding a source of these pre-existing solid particles is difficult [56], but in the F-layer the inner core could conceivably act as a source of fragments of iron. Furthermore, once some solid forms it could fragment and act to multiply the number density of particles, as seen in recent tank experiments [62].

Given this state of uncertainty, we propose a relatively simple approach to handling nucleation in our model. We imagine the presence of some pervasive ‘dust’ in the F-layer providing abundant sites for heterogeneous nucleation. We set $\gamma = 1.08 \text{ J m}^{-2}$ [57], $\theta = 5^\circ$ (appropriate for a metallic substrate) and treat I_0 as an adjustable parameter with which we can explore the behaviour of the slurry. Indeed, it turns out that the very rapid change in nucleation rate with I_0 allows us to tune the departure of the system from equilibrium and explore the ways a non-equilibrium slurry can behave. Incorporation of CNT as described above then means that the nucleation is turned off as the thermodynamic driving force decreases and increases with further departure from equilibrium.

5. A model of a slurry layer

The model developed in §3 describes a single iron snow particle falling through the F-layer, but it fails to capture several key aspects of the collective behaviour of iron particles and thus by itself is not capable of describing the F-layer as a whole. To make progress, we seek to build a simple model of the F-layer as a slurry. This model is designed to allow the consequences of the nucleation, growth and falling of the individual iron particles to be examined rather than to act as a definitive description of the F-layer. To construct this model, we imagine that solid particles can nucleate anywhere within the two-phase region before falling and growing until they ultimately settle on the ICB, contributing to inner core growth by sedimentation. As the particles grow, they exclude light elements and thus act as a source of oxygen and latent heat allowing the temperature and composition of the layer to change. A self-consistent solution for the temperature and liquid composition within the layer requires coupling between the particle-scale model developed here and a continuum theory for the transfer of heat and mass through a two-phase slurry. However, the general continuum theory is complex, is reliant on poorly known interaction parameters and, despite recent progress [20,63], is not fully developed for the two-component system. Therefore, to explore the possible behaviours of our model, we impose temperature and composition profiles inspired by previous equilibrium models [19] at the continuum scale. These profiles, shown in figure 1 are tied to a constant composition and adiabatic temperature profile in the outer core above the F-layer such that the first intersection with the liquidus occurs 200 km above the ICB. This defines the F-layer region where a two-phase slurry can exist. The temperature and compositional profiles inside the F-layer follow second-order polynomials with zero derivative at the ICB (because we assume no direct freezing on the ICB) leaving 1 d.f. for each profile: the temperature and composition at the ICB, which are described by ΔT_{ICB} and ΔX_{ICB} , respectively. In all cases, we require the temperature in the F-layer to be below the liquidus for the imposed composition as this is required to provide the thermodynamic driving force for nucleation or growth. Because of the imposed temperature and composition we describe the model as ‘quasi-steady state’ and note three important time-scales. We assume that changes to the solid-fraction in the layer happen more slowly than the short time needed for individual particles to nucleate, fall and grow described above (which means we can form averages over the lifetime of many individual particles). However, evolution of the temperature and composition happens more slowly than changes in the solid-fraction, with the slowest timescale presumably controlled by secular cooling of the whole outer core.

We discretize the F-layer into M radial layers of thickness $h = (R_F - R_{\text{ICB}})/M$ and N small equal area square patches which, at radius R , have area $A(R) = 4\pi R^2/N$. If $h \ll R$, the volume

of an element is $V(R) = A(R)h$ and the horizontal spacing between the middle of adjacent volume elements is given by $s_h(R) = \sqrt{A(R)}$. We note that the model only requires explicit consideration of one column of elements because we assume spherical symmetry for the F-layer. Given the volume of each element and the temperature, pressure and composition of the liquid imposed we are able to evaluate the average time between nucleation events in each volume element from [equation \(4.5\)](#). Assuming that the time needed for a particle to nucleate, fall and grow is much shorter than the timescale of changes in the temperature and composition of the layer, we can examine the behaviour of average particles and note that, on average, nucleation events will take place at the centre of the volume element and particles regularly nucleate at these points at times τ seconds apart. The subsequent evolution of each particle as it grows, falls and ultimately impacts the ICB is found by following the procedure described in §3c.

We describe the solid particles within the slurry in terms of their number density and size as functions of R . Our starting point is to calculate the vertical spacing between three particles nucleating in the same place in three consecutive nucleation events. These occur at time $t_0 - \tau$, t_0 and $t_0 + \tau$; all have initial radius r_0 (found from r_c in [equation \(4.2\)](#)) and, apart from this difference in the initial condition, the three particles will follow the same trajectory as the ICB. This means we can use $R_p(t; R_0, r_0)$, the solution to the coupled ODEs ([equations \(3.3\)](#) and [\(3.9\)](#)) giving the time evolution of the particle nucleating at R_0 , to find the vertical separation, s_v , between sequentially nucleating particles, given our ability to find $t(R_p)$ from the ODE solution:

$$s_v(R_p, R_0) = \frac{(R_p(t - \tau; R_0, r_0) - R_p(t; R_0, r_0)) + (R_p(t; R_0, r_0) - R_p(t + \tau; R_0, r_0))}{2}. \quad (5.1)$$

Here s_v depends on both the location where the separation is measured (i.e. the particle location, R_p) and on the location where the particles nucleated (R_0). [Equation \(5.1\)](#) relies on our quasi-steady-state assumption. At any location, there can be multiple populations of particles, of different sizes that nucleated in different places, falling past each other. Each population is represented by the solution of coupled ODEs with different initial conditions.

Particles spread out in space as they grow and fall faster. Counteracting this tendency to spread out vertically as they fall, streams of particles nucleating in horizontally adjacent volume elements will tend to approach each other due to the spherical geometry of the F-layer. The *partial* particle number density, that is, the contribution of the number of particles per unit volume at radius R_p arising from particles which initially nucleated from a nucleation volume centred at R_0 ($R_p < R_0$), is then

$$\bar{n}(R_p, R_0) = \frac{1}{s_v(R_p, R_0)s_h(R_p)^2}. \quad (5.2)$$

We can then find the total particle number density, $n(R_p)$, by summing the partial particle densities from nucleation points above R_p :

$$n(R_p) = \sum_{R_0=R_p}^{R_F} \bar{n}(R_p, R_0). \quad (5.3)$$

Here, the summation runs over all of the possible nucleation locations (R_0) above the location where the number density is being evaluated (R_p) because particles only fall downwards. This means that if $R_p = R_{\text{ICB}}$ there are M terms in the summation and if R_p is evaluated half way between the ICB and the top of the F-layer there are $M/2$ terms in the summation. Each term in the summation involves extracting results from solutions to the coupled ODEs with different initial conditions. The solid volume fraction at a given position can be calculated in a similar way noting that the different particle populations will have different radii depending on where they nucleate:

$$\phi(R_p) = \sum_{R_0=R_p}^{R_F} \bar{n}(R_p, R_0) \frac{4}{3} \pi r_p(t(R_p); R_0, r_0)^3, \quad (5.4)$$

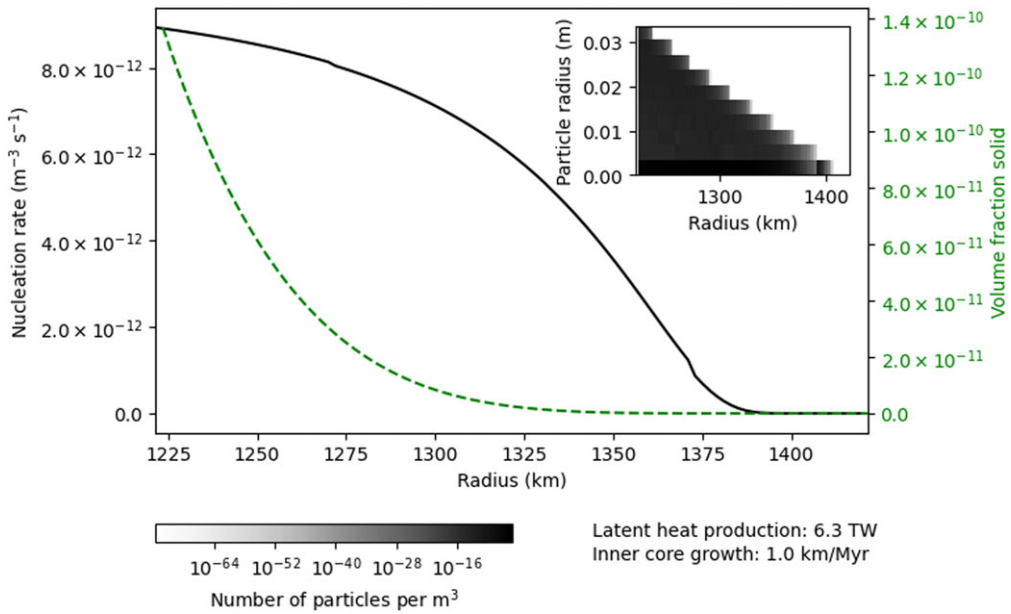


Figure 7. Key results from a slurry model of the F-layer with temperature and compositional profiles as shown in figure 1c, $D^L = 1 \times 10^{-9} \text{ m}^2 \text{ s}^{-1}$, $v^L = 2 \times 10^{-6} \text{ m}^2 \text{ s}^{-1}$ (corresponding to the light blue square in figure 5) and $I_0 = 1 \times 10^{-11} \text{ s}^{-1} \text{ m}^{-3}$. The main panel shows the calculated nucleation rate (black) and volume fraction solid (green), which both increase downwards as the under-cooling increases. Nucleation starts close to $R = 1375 \text{ km}$ where the temperature profile drops sufficiently below the liquidus (figure 1), but the very low undercooling results in such small nucleation and growth rates that the volume fraction solid remains effectively zero until $R = 1275 \text{ km}$ where the under-cooling becomes much more significant. The inset histogram of the number density of particles of different sizes as a function of depth reveals that once particles start to grow they grow steadily with the largest particles found just above the ICB. However, small particles that have not yet grown enough to fall quickly continue to dominate the particle size distribution throughout the layer.

again the summation runs over each possible nucleation location above R_p , and the product is between the number density of particles nucleating at R_0 (in m^{-3}) and their volume (in m^3). The mass fraction of solid is found considering the densities of the two phases:

$$\mathcal{M}(R_p) = \frac{\phi(R_p)\rho^S(R_p)}{\phi(R_p)\rho^S(R_p) + (1 - \phi(R_p))\rho^L(R_p)}. \quad (5.5)$$

Figure 7 shows the results of an example stratified F-layer with the imposed temperature and compositional profiles illustrated in figure 1 and material properties identical to those shown in light blue in figure 5. The under-cooling, and thus driving force for nucleation and growth, increases with depth yielding an increasing nucleation rate and solid fraction from the top to the bottom of the F-layer. The inset histogram of particle size distribution as a function of radius shows that in all cases the particle population is dominated by a large number of very small particles. These are recently nucleated and have not yet grown enough to fall quickly, corresponding to the early parts of the trajectories shown in figure 5a. The largest particles in the population increase in radius downwards, reflecting the increased time available for growth of particles nucleating near the top of the layer, and the largest particles in the whole layer are found just above the ICB. These particles nucleated near the top of the layer and are the oldest particles as well as the largest and most rapidly falling. Maximum particle radii are smaller than the single particle cases described in §3c because the under-cooling goes to zero at the top of the F-layer (so growth is slower).

The results of the model also give access to properties related to the thermal history of the Earth. These depend on the total growth rate of solid at a given radius within the F-layer. This Lagrangian derivative is found by finite difference of the particle radii:

$$\dot{\phi}(R_p) = \frac{d\phi(R_p)}{dt} \approx \sum_{R_0=R_p}^{R_F} \bar{n}(R_p, R_0) \frac{4\pi}{3} \frac{r_p(t(R_p) + \Delta t; R_0, r_0)^3 - r_p(t(R_p) - \Delta t; R_0, r_0)^3}{2\Delta t}, \quad (5.6)$$

where the summation runs over each possible nucleation location above R_p (see equation (5.3)); $\dot{\phi}(R_p)$ gives access to the rate of change of solid mass fraction:

$$\dot{\mathcal{M}}(R_p) = \frac{\dot{\phi}(R_p) \rho^S(R_p) \rho^L(R_p)}{(\phi(R_p) \rho^S(R_p) + (1 - \phi(R_p)) \rho^L(R_p))^2}. \quad (5.7)$$

Growth of solid results in the release of latent heat where the specific latent heat of crystallization, L , is taken as 750 kJ kg^{-1} [32]. Integrating over the F-layer gives the total heat production rate due to formation of solid in the layer, which we equate to the heat flux out of the layer because we assume a fixed layer temperature:

$$Q^F = 4\pi \int_{R_{\text{ICB}}}^{R_F} \dot{\mathcal{M}}(R) \rho^S(R) L R^2 dR. \quad (5.8)$$

Finally, we calculate the rate of predicted inner core growth from sedimentation by evaluating the rate at which solid arrives at the ICB given its surface area:

$$G_{\text{ICB}} = \frac{1}{4\pi R_{\text{ICB}}^2} \int_{R_{\text{ICB}}}^{R_F} \frac{I(R)}{2} \cdot \frac{4}{3} \pi r_p(R_{\text{ICB}}; R, r_0)^3 \cdot 4\pi R^2 dR. \quad (5.9)$$

Equation (5.9) does not rely on the assumption of a quasi-steady state, only that all particles that nucleate reach the ICB on the timescale of inner core growth. Values for Q^F and G_{ICB} calculated for our example simulation are given in figure 7.

6. Plausible non-equilibrium models of the F-layer

We now search for model parameters that are consistent with geophysical observations, and outline the resulting model outputs for plausible F-layer configurations. For the Earth, our models must obey some important constraints. An inner core age in the range 0.5–1.5 Gyr gives mean growth rates in the range $0.8\text{--}2.4 \text{ km Myr}^{-1}$ [32]. However, this estimate includes the effect of direct freezing at the interface, which is not accounted for in our model, and is therefore an upper bound on the allowed growth rate. The latent heat production is more tightly constrained for the Earth as it cannot exceed the total heat Q^c leaving the core. Estimates of Q^c are usually in the range 5–17 TW [1,64] and are unlikely to exceed 20 TW [65]. However, given that secular cooling contributes at least 4 TW [66], and more likely approximately 6 TW [67], and gravitational energy another 2–4 TW, the latent heat contribution is expected to be approximately 6 TW and no larger than 10 TW [67]. We note that the constraints on plausible values for Q^F and G_{ICB} are not forced to be consistent as they are based on different observations that may relate to different time periods. However, we can estimate the latent heat released for a given inner core growth rate. A G_{ICB} between 0.8 and 2.4 km Myr^{-1} implies Q^F between 4.5 and 13.6 TW, which is broadly consistent of the our independent estimate of Q^F . On the basis of these estimates, the combination of physical properties with thermal and compositional profiles shown in figure 7 produces a ‘viable’ non-equilibrium model of a slurry with Q^F and G_{ICB} within the expected range.

In figure 8a, we investigate the model behaviour by changing the imposed temperature or composition profiles, which are parametrized by ΔT_{ICB} and ΔX_{ICB} , respectively (figure 1). Here ΔT_{ICB} is the difference in temperature between an extrapolated adiabat (defined so as to intersect the liquidus at the top of the F-layer 200 km above the ICB) and the temperature at the ICB, while ΔX_{ICB} is the difference in composition between the well-mixed convecting outer core (which always has 17 mol% oxygen) and the F-layer just above the ICB (negative values imply oxygen

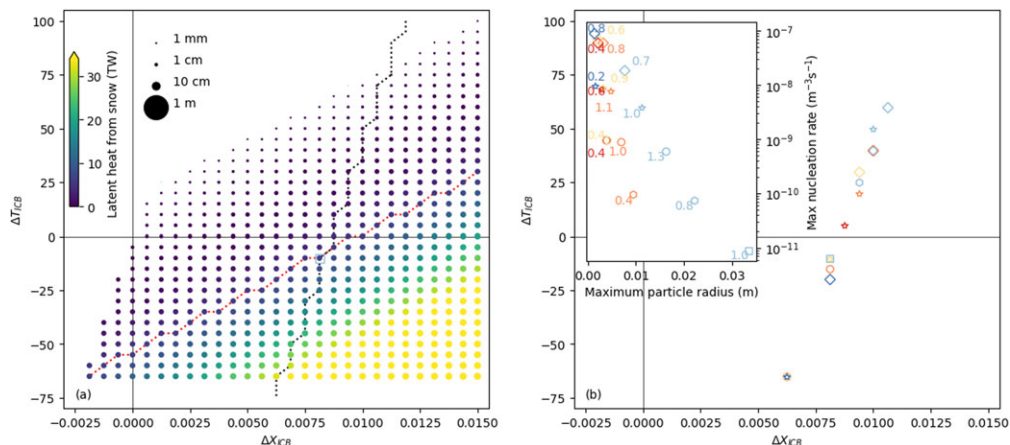


Figure 8. Gross properties of models of the F-layer. (a) Models with fixed material properties corresponding to the model shown in figure 7 but with different thermal and compositional profiles as defined by ΔT_{ICB} and ΔX_{ICB} (figure 1). Symbol size represents the largest particle size and colour represents the latent heat released by the layer. The black dashed line connects model cases where the slurry is approximately 27.24 kg m^{-3} denser than the extrapolated adiabat at the ICB and the red dashed line connects models releasing approximately 6 TW of latent heat. The model highlighted by a blue square is shown in figure 7. (b) Locus of temperature and compositional profiles which result in successful models (27.24 kg m^{-3} excess density and 6 TW of latent heat) for the different material properties. Symbol colours indicate D^L and v^L pairs (matching the colours used in figure 5) and symbol shapes representing different nucleation pre-factors (diamonds, $I_0 = 1 \times 10^{-7}$; stars, $I_0 = 1 \times 10^{-8}$; circles, $I_0 = 1 \times 10^{-9}$; hexagons, $I_0 = 1 \times 10^{-10}$; squares, $I_0 = 1 \times 10^{-11} \text{ s}^{-1} \text{ m}^{-3}$). The inset shows the relationship between maximum particle radius and nucleation rate for these successful cases with the numerals indicating the inner core growth rate in km Myr^{-1} . Model inputs and outputs are tabulated in the electronic supplementary material.

enrichment). We limit the parameter space by requiring that: (i) the temperature increases with depth in the F-layer, as suggested by previous models [6,19] and is below the liquidus at the ICB as required for slurry solutions; (ii) oxygen depletion at the ICB is at most 1.5% compared with the overlying outer core ($\Delta X_{ICB} \leq 0.015$) as suggested by the results of [19]; the liquid is stably stratified ($N_{BW}^2 < 0$). These constraints confine solutions to the region encompassed by points in figure 8a with the upper boundary representing the liquidus and the left-hand boundary representing the stability constraint. Stratified models can exist in regions where the liquid is enriched or depleted in oxygen compared with the overlying well-mixed outer core and in regions where the temperature is higher than or lower than the temperature of the adiabat projected to the ICB. Increasing the distance from equilibrium (increasing ΔX_{ICB} or decreasing ΔT_{ICB}) drives larger \dot{M} from growth and nucleation, leading to larger r_p and higher Q^F . Both values are approximately constant along lines parallel to the liquidus (i.e. lines of constant $\Delta \mu_{Fe}$). The maximum size of crystals saturates in the centimetre range because of the increased falling speed of large crystals discussed in §3. The latent heat production increases exponentially with increasing $\Delta \mu_{Fe}$ (the colour scale is saturated at Earth's surface heat flux), which is presumably driven by the nucleation rate.

Although figure 8a shows a wide range of compositions and temperatures for an F-layer configuration where a slurry could exist, the range of models that are consistent with geophysical constraints on the present-day F-layer are more limited. We choose two particular observations to winnow out Earth-like models from within the wedge of slurry models. First, we demand that the density difference between an outer core adiabat extrapolated to the ICB and the density of the slurry layer (including effects of temperature, composition, and solid fraction) matches the difference between PREM and AK135f such that models have an excess density of 27.24 kg m^{-3} . This essentially seismological constraint is represented by the black dashed line in figure 8a. In all such cases, we find a low amount of solid and that the excess density is predominantly caused the

fact that $\Delta X_{\text{ICB}} > 0$. We also consider the heat produced by the layer. This must certainly be less than Earth's surface heat flux, indicated by the yellow saturation in figure 8a, but as discussed above, is probably closer to 6 TW, the value indicated by the red dashed line. In figure 8a, these lines cross and we consider the model where these two constraints are met as 'Earth like', and it is that model that is shown in figure 7. We emphasize that these choices are illustrative and do not capture the full range of possible Earth-like models where the excess density and latent heat production, as well as the composition and temperature of the overlying outer core could all differ from the models illustrated here.

Figure 8b shows the properties of Earth-like slurry solutions in $\Delta X_{\text{ICB}}-\Delta T_{\text{ICB}}$ space as a function of the nucleation pre-factor (shown as different symbol shapes), viscosity and oxygen diffusivity of the liquid (shown as different symbol colours). Changing these properties does not alter the density of the slurry (because the density difference is dominated by the density of the liquid, not the solid fraction, which is always low) so successful models plot along a common line in $\Delta X_{\text{ICB}}-\Delta T_{\text{ICB}}$ space. Material properties that give higher solid production rates (e.g. caused by increasing the nucleation pre-factor or the diffusion coefficient) yield solutions that are closer to the liquidus at the ICB (smaller $\Delta\mu_{\text{Fe}}$, larger positive ΔT_{ICB}), while properties that slow the solid production rate (e.g. decreasing the pre-factor or the diffusion rate) yield solutions that are further from the liquidus as they need larger $\Delta\mu_{\text{Fe}}$ (and thus negative ΔT_{ICB}) to drive solid formation. The models have different maximum particle sizes, though all are dominated by a population of very small slowly falling particles, with the largest particles only reaching millimetre to centimetre sizes before they leave the layer. The predicted inner core growth rates ($0.4\text{--}1.3\text{ km Myr}^{-1}$) are below the maximum permitted growth rate assuming a young inner core growing at a constant rate. This is expected because we do not include direct freezing at the ICB, and our growth-rate estimates are therefore consistent with other geophysical inferences.

Overall, we find significant diversity of Earth-like slurry models of the F-layer where we do not need to carefully tune model parameters such as viscosity or light element diffusivity to match the expected heat production rate and density stratification for a low-volume fraction slurry. By contrast, we are unable to produce viable models assuming homogeneous nucleation of solid particles to form the slurry and do need to resort to alternative physical mechanisms where the nucleation rate effectively acts as a tuning parameter. In all cases, excess Fe in the liquid (0.6–1.06 mol.% compared with the overlying well-mixed core) is the dominant direct cause of the density anomaly rather than the presence of solid particles. This is reassuring as it both accords with our assumption that the falling particles do not interact, and matches the predictions of previous equilibrium models. Indeed, our results yield much lower solid volume fractions ($1 \times 10^{-10} - 1 \times 10^{-11}$) than equilibrium models (e.g. less than 0.05 [20]) as expected given that nucleation and growth must cease as the system approaches equilibrium. In terms of temperature, valid models can be sub- or super-adiabatic with the degree of under-cooling compared with the liquidus (approx. 35–150 K) required to drive crystal growth increasing as the intrinsic nucleation or growth rate decreases. This estimate of the undercooling required for nucleation complements previous independent inferences from mineralogical [59,60] and geodynamic [68] modelling and is lower than the maximum undercooling allowed by the present-day thermal structure of the core [56,69].

7. Conclusion

Our 'bottom-up' construction of a model of a core slurry layer, focusing on processes that control the nucleation, growth and settling of isolated solid particles, has allowed us to explore the evolution of single particles in a two-phase system. One important feature of this approach is that the temperature must depart from the liquidus temperature to allow the solid to form, something that is forbidden in equilibrium models. Building a quasi-steady-state model of the whole slurry layer allows us to describe the number density, longevity and size distribution of particles within the layer. These properties are inaccessible (without additional assumption) in equilibrium models, which only predict the volume fraction solid. We have applied this model

to the Earth's F-layer for a particular choice of Fe–O chemistry and varied the temperature and composition in the F-layer along with the intrinsic material properties of iron (the oxygen diffusivity, viscosity and nucleation pre-factor). Even within this restricted model space we find a diversity of potential slurry models that are consistent with inferred properties of the F-layer and the heat budget of the core. In all cases, models are dominated by a large number of small, slowly falling particles with a handful of the largest particles being limited to centimetre size. In common with equilibrium models, the solid fraction is always small, and it is the chemistry of the liquid that dominates the density structure of the layer.

One way to view our approach is as a framework to describe non-equilibrium processes that must operate in a core slurry layer. The framework incorporates micro-scale processes from fluid dynamics and mineral physics into a simple model of the whole slurry layer to probe core-scale processes that can be interrogated by seismology. The representation is designed to be flexible: alternative thermodynamic models containing different light elements can be used as long as the relevant chemical potentials are available, while different scaling laws for particle dynamics and parametrizations for nucleation and growth rate can be swapped for those chosen here. One caveat is our assumption that light elements do not enter the solid phase: lifting this assumption would be challenging because this would necessitate tracking the chemistry of the solid particles as they fall. Nevertheless, the model framework is sufficiently general that it could be readily adapted to represent snow zones in other terrestrial planetary cores.

Immediate extensions to our work include the need to compare outputs with a wider range of geophysical observations and consider different outer core adiabats and chemistries, as well as including the possibility of some direct freezing on the inner core. This would imply the need to alter the temperature and compositional profile imposed on the F-layer to capture the release of latent heat and light elements associated with direct freezing. Including direct freezing would also alter the growth and nucleation rate of solid particles within the slurry layer. It is also desirable to produce solutions where the temperature and composition are not imposed, but solved self-consistently. This could be achieved by coupling our particle-based framework to a continuum model of two-component non-equilibrium slurry dynamics. However, this is non-trivial as it would be necessary to capture the heat and chemical fluxes through the layer and, in a slurry, there is a necessary advection of heat and chemical components by fluid flow and this fluid flow would affect the falling velocity of the particles. We imagine that such an approach would necessitate using velocities and densities of the falling particles to evaluate the velocity of fluid flow before iterating to find particle falling velocities and growth rates that are consistent with the resulting fluid flow. Eventually, this should result in a model where the temperature, composition, particle density and particle falling rates are all consistent with each other. Our expectation is that such an exercise would require significant work to make the coupled model theoretically and practically viable.

Data accessibility. All software used to create the models described in this submission is openly available on GitHub (<https://github.com/andreww/slurry>) with a permanent snapshot archived with Zenodo [70]. This software includes code used to create all figures and results in the paper. The data are provided in electronic supplementary material [71].

Declaration of AI use. We have not used AI-assisted technologies in creating this article.

Authors' contributions. A.M.W.: conceptualization, data curation, formal analysis, funding acquisition, investigation, methodology, resources, software, visualization, writing—original draft, writing—review and editing; C.J.D.: conceptualization, formal analysis, funding acquisition, investigation, project administration, resources, writing—original draft, writing—review and editing; A.J.W.: formal analysis, investigation, methodology, validation, visualization, writing—original draft; M.I.B.: conceptualization, formal analysis, investigation, methodology, validation, visualization, writing—review and editing.

All authors gave final approval for publication and agreed to be held accountable for the work performed therein.

Conflict of interest declaration. We declare we have no competing interests.

Funding. All authors gratefully acknowledge support from the NERC seedcorn grant 'Non-equilibrium thermodynamics in Earth's core – the agenda for the next decade' (reference NE/T004835/1). C.D. and F.W. additionally acknowledge support from NERC (grant nos NE/V010867/1 and NE/T000228/1).

Acknowledgements. We thank R. Deguen and an anonymous reviewer for helpful comments on this manuscript. For the purpose of Open Access, the authors have applied a CC BY public copyright licence to any Author Accepted Manuscript (AAM) version arising from this submission.

References

1. Nimmo F. 2015 Energetics of the core. In *Treatise on geophysics*, vol. 8, pp. 27–55. Amsterdam, The Netherlands: Elsevier. (doi:10.1016/B978-0-444-53802-4.00139-1)
2. Bergman MI. 1997 Measurements of electric anisotropy due to solidification texturing and the implications for the Earth's inner core. *Nature* **389**, 60–63. (doi:10.1038/37962)
3. Alboussiere T, Deguen R, Melzani M. 2010 Melting-induced stratification above the Earth's inner core due to convective translation. *Nature* **466**, 744–747. (doi:10.1038/nature09257)
4. Deguen R, Olson P, Reynolds E. 2014 F-layer formation in the outer core with asymmetric inner core growth. *C. R. Geosci.* **346**, 101–109. (doi:10.1016/j.crte.2014.04.003)
5. Deguen R, Alboussiere T, Labrosse S. 2018 Double-diffusive translation of Earth's inner core. *Geophys. J. Int.* **214**, 88–107. (doi:10.1093/gji/ggy120)
6. Gubbins D, Masters G, Nimmo F. 2008 A thermochemical boundary layer at the base of Earth's outer core and independent estimate of core heat flux. *Geophys. J. Int.* **174**, 1007–1018. (doi:10.1111/j.1365-246X.2008.03879.x)
7. Wong J, Davies CJ, Jones CA. 2018 A Boussinesq slurry model of the F-layer at the base of Earth's outer core. *Geophys. J. Int.* **214**, 2236–2249. (doi:10.1093/gji/ggy245)
8. Hauck SA, Aurnou JM, Dombard AJ. 2006 Sulfur's impact on core evolution and magnetic field generation on Ganymede. *J. Geophys. Res.* **111**, E09008. (doi:10.1029/2005JE002557)
9. Stewart AJ, Schmidt MW, van Westrenen W, Liebske C. 2007 Mars: a new core-crystallization regime. *Science* **316**, 1323–1325. (doi:10.1126/science.1140549)
10. Rückriemen T, Breuer D, Spohn T. 2015 The Fe snow regime in Ganymede's core: a deep-seated dynamo below a stable snow zone. *J. Geophys. Res.: Planets* **120**, 1095–1118. (doi:10.1002/2014JE004781)
11. Dumberry M, Rivoldini A. 2015 Mercury's inner core size and core-crystallization regime. *Icarus* **248**, 254–268. (doi:10.1016/j.icarus.2014.10.038)
12. Davies CJ, Pommier A. 2018 Iron snow in the Martian core? *Earth Planet. Sci. Lett.* **481**, 189–200. (doi:10.1016/j.epsl.2017.10.026)
13. Edgington A, Vočadlo L, Stixrude L, Wood I, Dobson D, Holmström E. 2019 The top-down crystallisation of Mercury's core. *Earth Planet. Sci. Lett.* **528**, 115838. (doi:10.1016/j.epsl.2019.115838)
14. Williams Q. 2009 Bottom-up versus top-down solidification of the cores of small solar system bodies: constraints on paradoxical cores. *Earth Planet. Sci. Lett.* **284**, 564–569. (doi:10.1016/j.epsl.2009.05.019)
15. Loper DE, Roberts PH. 1981 A study of conditions at the inner core boundary of the earth. *Phys. Earth Planet. Inter.* **24**, 302–307. (doi:10.1016/0031-9201(81)90117-5)
16. Loper DE, Roberts PH. 1987 Boussinesq model of a slurry. In *Structure and dynamics of partially solidified systems* (ed. DE Loper). NATO Advanced Sciences Institute Series E: Applied Sciences, pp. 293–322. Martinus Nijhoff.
17. Loper DE, Roberts PH. 1977 On the motion of an iron-alloy core containing a slurry: I. General theory. *Geophys. Astrophys. Fluid Dyn.* **9**, 289–321. (doi:10.1080/03091927708242333)
18. Zhang Y, Nelson P, Dygert N, Lin JF. 2019 Fe alloy slurry and a compacting cumulate pile across Earth's inner-core boundary. *J. Geophys. Res.: Solid Earth* **124**, 10954–10967. (doi:10.1029/2019JB017792)
19. Wong J, Davies CJ, Jones CA. 2021 A regime diagram for the slurry F-layer at the base of Earth's outer core. *Earth Planet. Sci. Lett.* **560**, 116791. (doi:10.1016/j.epsl.2021.116791)
20. Wilczyński F, Davies CJ, Jones CA. 2023 A two-phase pure slurry model for planetary cores: one-dimensional solutions and implications for Earth's F-layer. *J. Fluid Mech.* **976**, A5. (doi:10.1017/jfm.2023.834)
21. Song X, Helmberger DV. 1992 Velocity structure near the inner core boundary from waveform modeling. *J. Geophys. Res.: Solid Earth* **97**, 6573–6586. (doi:10.1029/92JB00330)
22. Kennett BL, Engdahl E, Buland R. 1995 Constraints on seismic velocities in the Earth from traveltimes. *J. Geophys. J. Int.* **122**, 108–124. (doi:10.1111/j.1365-246X.1995.tb03540.x)

23. Souriau A, Poupinet G. 1991 The velocity profile at the base of the liquid core from PKP(BC+Cdiff) data: an argument in favour of radial inhomogeneity. *Geophys. Res. Lett.* **18**, 2023–2026. (doi:10.1029/91GL02417)
24. Souriau A, Roudil P. 1995 Attenuation in the uppermost inner core from broad-band GEOSCOPE PKP data. *Geophys. J. Int.* **123**, 572–587. (doi:10.1111/j.1365-246X.1995.tb06872.x)
25. Song X, Helmberger D. 1995 A *P* wave model of Earth's core. *J. Geophys. Res.: Solid Earth* **100**, 9817–9830. (doi:10.1029/94JB03135)
26. Zou Z, Koper KD, Cormier VF. 2008 The structure of the base of the outer core inferred from seismic waves diffracted around the inner core. *J. Geophys. Res.* **113**, B05314. (doi:10.1029/2007JB005316)
27. Ohtaki T, Kaneshima S. 2015 Independent estimate of velocity structure of Earth's lowermost outer core beneath the northeast Pacific from PKiKP–PKPbc differential traveltime and dispersion in PKPbc. *J. Geophys. Res.: Solid Earth* **120**, 7572–7586. (doi:10.1002/2015JB012140)
28. Souriau A, Calvet M. 2015 Deep earth structure: the Earth's cores. In *Treatise on geophysics*, vol. 1, pp. 725–757. Amsterdam, The Netherlands: Elsevier. (doi:10.1016/B978-0-444-53802-4.00020-8)
29. Dziewonski AM, Anderson DL. 1981 Preliminary reference Earth model. *Phys. Earth Planet. Inter.* **25**, 297–356. (doi:10.1016/0031-9201(81)90046-7)
30. Pozzo M, Davies CJ, Alfè D. 2022 Towards reconciling experimental and computational determinations of Earth's core thermal conductivity. *Earth Planet. Sci. Lett.* **584**, 117466. (doi:10.1016/j.epsl.2022.117466)
31. Frost D, Lasbleis M, Chandler B, Romanowicz B. 2021 Dynamic history of the inner core constrained by seismic anisotropy. *Nat. Geosci.* **14**, 531–535. (doi:10.1038/s41561-021-00761-w)
32. Davies C, Pozzo M, Gubbins D, Alfè D. 2015 Constraints from material properties on the dynamics and evolution of Earth's core. *Nat. Geosci.* **8**, 678–685. (doi:10.1038/ngeo2492)
33. Gubbins D, Sreenivasan B, Mound J, Rost S. 2011 Melting of the Earth's inner core. *Nature* **473**, 361–363. (doi:10.1038/nature10068)
34. Solomatov VS, Stevenson DJ. 1993 Kinetics of crystal growth in a terrestrial magma ocean. *J. Geophys. Res.: Planets* **98**, 5407–5418. (doi:10.1029/92JE02839)
35. Loper DE. 1992 A nonequilibrium theory of a slurry. *Continuum Mech. Thermodyn.* **4**, 213–245. (doi:10.1007/BF01130292)
36. Alfè D, Gillan MJ, Price GD. 2002 Complementary approaches to the *ab initio* calculation of melting properties. *J. Chem. Phys.* **116**, 6170–6177. (doi:10.1063/1.1460865)
37. Alfè D, Gillan M, Price G. 2007 Temperature and composition of the Earth's core. *Contemp. Phys.* **48**, 63–80. (doi:10.1080/00107510701529653)
38. Komabayashi T. 2014 Thermodynamics of melting relations in the system Fe–FeO at high pressure: implications for oxygen in the Earth's core. *J. Geophys. Res.: Solid Earth* **119**, 4164–4177. (doi:10.1002/2014JB010980)
39. Etter M, Dinnebier RE. 2014 Direct parameterization of the pressure-dependent volume by using an inverted approximate Vinet equation of state. *J. Appl. Crystallogr.* **47**, 384–390. (doi:10.1107/S1600576713032287)
40. Rückriemen T, Breuer D, Spohn T. 2018 Top-down freezing in a Fe–FeS core and Ganymede's present-day magnetic field. *Icarus* **307**, 172–196. (doi:10.1016/j.icarus.2018.02.021)
41. Pozzo M, Davies C, Gubbins D, Alfè D. 2013 Transport properties for liquid silicon-oxygen-iron mixtures at Earth's core conditions. *Phys. Rev. B* **87**, 014110. (doi:10.1103/PhysRevB.87.014110)
42. Clift R, Gauvin W. 1970 The motion of particles in turbulent gas streams. In *Chemeca 70: A Conference Convened by the Australian National Committee of the Institution of Chemical Engineers and the Australian Academy of Science*, pp. 14–28. Chatswood, N.S.W.: Butterworths and the Institution of Chemical Engineers.
43. Clift R, Gauvin W. 1971 Motion of entrained particles in gas streams. *Can. J. Chem. Eng.* **49**, 439–448. (doi:10.1002/cjce.5450490403)
44. Zhang Y, Xu Z. 2003 Kinetics of convective crystal dissolution and melting, with applications to methane hydrate dissolution and dissociation in seawater. *Earth Planet. Sci. Lett.* **213**, 133–148. (doi:10.1016/S0012-821X(03)00297-8)
45. Inman BG, Davies CJ, Torres CR, Franks PJS. 2020 Deformation of ambient chemical gradients by sinking spheres. *J. Fluid Mech.* **892**, A33. (doi:10.1017/jfm.2020.191)
46. Grossmann S, Lohse D. 2000 Scaling in thermal convection: a unifying theory. *J. Fluid Mech.* **407**, 27–56. (doi:10.1017/S0022112099007545)

47. Montagner JP, Kennett BLN. 1996 How to reconcile Body-Wave and Normal-Mode reference Earth models. *Geophys. J. Int.* **125**, 229–248. (doi:10.1111/j.1365-246X.1996.tb06548.x)
48. Wilson HW. 1900 On the velocity of solidification and viscosity of super-cooled liquids. *Philos. Mag.* **50**, 238–250. (doi:10.1080/14786440009463908)
49. Frenkel J. 1946 *Kinetic theory of liquids*. Oxford, UK: Oxford University Press.
50. Coriell S, Turnbull D. 1982 Relative roles of heat transport and interface rearrangement rates in the rapid growth of crystals in undercooled melts. *Acta Metall.* **30**, 2135–2139. (doi:10.1016/0001-6160(82)90134-1)
51. Mikheev L, Chernov A. 1991 Mobility of a diffuse simple crystal–melt interface. *J. Cryst. Growth* **112**, 591–596. (doi:10.1016/0022-0248(91)90340-B)
52. Sun G, Xu J, Harrowell P. 2018 The mechanism of the ultrafast crystal growth of pure metals from their melts. *Nat. Mater.* **17**, 881–886. (doi:10.1038/s41563-018-0174-6)
53. Shampine LF. 1986 Some practical Runge–Kutta formulas. *Math. Comput.* **46**, 135–150. (doi:10.1090/S0025-5718-1986-0815836-3)
54. Virtanen P et al. 2020 SciPy 1.0: fundamental algorithms for scientific computing in Python. *Nat. Methods* **17**, 261–272. (doi:10.1038/s41592-019-0686-2)
55. Christian JW. 2002 *The theory of transformations in metals and alloys*. Oxford, UK: Pergamon Press.
56. Huguet L, Van Orman JA, Hauck SA, Willard MA. 2018 Earth's inner core nucleation paradox. *Earth Planet. Sci. Lett.* **487**, 9–20. (doi:10.1016/j.epsl.2018.01.018)
57. Davies CJ, Pozzo M, Alfè D. 2019 Assessing the inner core nucleation paradox with atomic-scale simulations. *Earth Planet. Sci. Lett.* **507**, 1–9. (doi:10.1016/j.epsl.2018.11.019)
58. Shimizu H, Poirier J, Le Mouél J. 2005 On crystallization at the inner core boundary. *Phys. Earth Planet. Inter.* **151**, 37–51. (doi:10.1016/j.pepi.2005.01.001)
59. Wilson AJ, Walker AM, Alfè D, Davies CJ. 2021 Probing the nucleation of iron in Earth's core using molecular dynamics simulations of supercooled liquids. *Phys. Rev. B* **103**, 214113. (doi:10.1103/PhysRevB.103.214113)
60. Sun Y, Zhang F, Mendelev MI, Wentzcovitch RM, Ho KM. 2022 Two-step nucleation of the Earth's inner core. *Proc. Natl Acad. Sci. USA* **119**, e2113059119. (doi:10.1073/pnas.2113059119)
61. Alfred W, Andrew W, Dario A, Christopher D. 2023 Can homogeneous nucleation resolve the inner core nucleation paradox? *Earth Planet. Sci. Lett.* **614**, 118176. (doi:10.1016/j.epsl.2023.118176)
62. Huguet L, Le Bars M, Deguen R. 2023 A laboratory model for iron snow in planetary cores. *Geophys. Res. Lett.* **50**, e2023GL105697. (doi:10.1029/2023GL105697)
63. Bercovici D, Mulyukova E. 2020 Two-phase magnetohydrodynamics: theory and applications to planetesimal cores. *Phys. Earth Planet. Inter.* **300**, 106432. (doi:10.1016/j.pepi.2020.106432)
64. Jaupart C, Labrosse S, Lucazeau F, Mareschal JC. 2015 Temperatures, heat, and energy in the Mantle of the earth. In *Treatise on geophysics*, vol. 5, pp. 254–298. Amsterdam, The Netherlands: Elsevier. (doi:10.1016/B978-0-444-53802-4.00126-3)
65. Frost DA, Avery MS, Buffett BA, Chidester BA, Deng J, Dorfman SM, Li Z, Liu L, Lv M, Martin JF. 2022 Multidisciplinary constraints on the thermal-chemical boundary between Earth's core and mantle. *Geochem. Geophys. Geosyst.* **23**, e2021GC009764. (doi:10.1029/2021GC009764)
66. Gubbins D, Alfè D, Masters G, Price GD, Gillan M. 2004 Gross thermodynamics of two-component core convection. *Geophys. J. Int.* **157**, 1407–1414. (doi:10.1111/j.1365-246X.2004.02219.x)
67. Davies CJ. 2015 Cooling history of Earth's core with high thermal conductivity. *Phys. Earth Planet. Inter.* **247**, 65–79. (doi:10.1016/j.pepi.2015.03.007)
68. Lasbleis M, Kervazo M, Choblet G. 2020 The fate of liquids trapped during the Earth's inner core growth. *Geophys. Res. Lett.* **47**, e2019GL085654. (doi:10.1029/2019GL085654)
69. Wilson AJ, Alfè D, Walker AM, Davies CJ. 2023 Can homogeneous nucleation resolve the inner core nucleation paradox? *Earth Planet. Sci. Lett.* **614**, 118176. (doi:10.1016/j.epsl.2023.118176)
70. Walker A, Davies C, FWilson93. 2025 andreww/slurry: v1.0.0 (v1.0.0). *Zenodo*. (doi:10.5281/zenodo.14918170)
71. Walker AM, Davies CJ, Wilson AJ, Bergman MI. 2025 A non-equilibrium slurry model for planetary cores with application to Earth's F-layer. *Figshare*. (doi:10.6084/m9.figshare.c.7719725)